

Edge-based fever screening system over private 5G

Murugan Sankaradas, Kunal Rao, Ravi Rajendran, Amit Redkar and Srimat Chakradhar
 NEC Laboratories America, Inc.
 Princeton, NJ

Abstract—Edge computing and 5G have made it possible to perform analytics closer to the source of data and achieve super-low latency response times, which isn't possible with centralized cloud deployment. In this paper, we present a novel fever screening system, which uses edge machine learning techniques and leverages private 5G to accurately identify and screen individuals with fever in real-time. Particularly, we present deep-learning based novel techniques for fusion and alignment of cross-spectral visual and thermal data streams at the edge. Our novel Cross-Spectral Generative Adversarial Network (CS-GAN) synthesizes visual images that have the key, representative object level features required to uniquely associate objects across visual and thermal spectrum. Two key features of CS-GAN are a novel, feature-preserving loss function that results in high-quality pairing of corresponding cross-spectral objects, and dual bottleneck residual layers with skip connections (a new, network enhancement) to not only accelerate real-time inference, but to also speed up convergence during model training at the edge. To the best of our knowledge, *this is the first technique that leverages 5G networks and limited edge resources to enable real-time feature-level association of objects in visual and thermal streams (30 ms per full HD frame on an Intel Core i7-8650 4-core, 1.9GHz mobile processor)*. To the best of our knowledge, this is also *the first system to achieve real-time operation, which has enabled fever screening of employees and guests in arenas, theme parks, airports and other critical facilities*. By leveraging edge computing and 5G, our fever screening system is able to achieve 98.5% accuracy and is able to process $\sim 5X$ more people when compared to a centralized cloud deployment.

Index Terms—Edge computing, 5G, fever screening, cross spectral streams, stream fusion

I. INTRODUCTION

Fever is a very common symptom for various infectious diseases like COVID-19. Identifying and isolating individuals with fever, before they come in contact with others, helps in reducing the transmission and spread of the virus. Accurate fever detection requires measuring temperature at the inner canthus of the eye. To do this without human intervention, sensors with visual and thermal camera are deployed. Visual camera feed is used to identify inner canthus region while thermal camera feed is used to obtain the temperature at this region.

Fig. 1 shows an overview of fever screening system to detect elevated body temperature of persons entering facilities like factories, office complexes, schools, etc. Visual and thermal feed is transmitted over private 5G network, which has high bandwidth and low latency, and all analytics is performed on the edge computing infrastructure, which avoids the delays incurred in moving raw data streams to the cloud over poor bandwidth and high latency network.

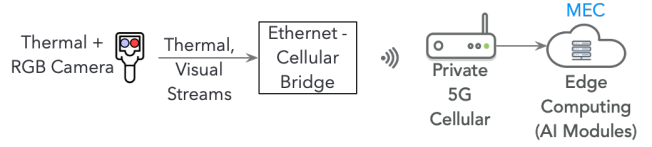


Figure 1: Fever screening system overview

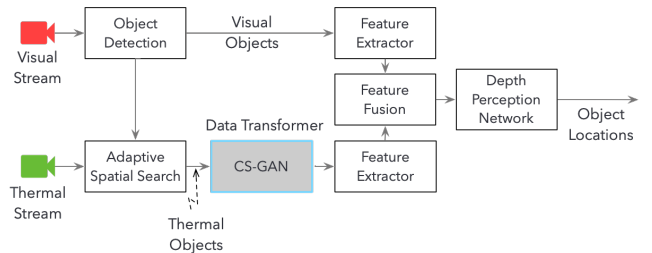


Figure 2: Overview of AI Modules in Edge System

One thing to note is that the visual and thermal cameras are disparate and placed right next to each other, which makes them have slightly different view point. Due to this, both the streams have to be fused in real-time to measure the temperature accurately and for this, we use edge machine learning techniques. The measured temperature also varies depending on the distance from the sensors. Farther the distance, lesser is the measured temperature because gases and particles in the atmosphere absorb some of the emitted infrared radiation. Therefore, our system detects individuals and estimates their depth and offset in real-time to compensate for this variation. Fusing multiple sensor streams is a non-trivial task. *First*, fields of view are not aligned due to the physical displacement of the sensors. *Second*, the semantic information and data formats of the sensors are radically different [1]. *Third*, cross-spectral object localization and depth perception under application-specific affordable cost and resource constraints is a major challenge. Our key contributions in this paper are:

- A new cross-spectral deep-learning generative adversarial network CS-GAN that synthesizes feature preserving images from thermal data, to perform real-time object feature-level association in visual and thermal streams at the edge (30 ms per full HD frame on i7-8650 CPU).
- A new multivariable linear regression model, to estimate location using object's feature-level correspondence.
- A novel edge-based fever screening system, which uses CS-GAN to associate objects in visual and thermal streams, and measures temperatures of individuals in realtime.

Experimental results show that our fever screening system,

running at the edge, is able to achieve 98.5% accuracy and process $\sim 5X$ more people per minute compared to a centralized cloud deployment.

II. PROPOSED APPROACH

Fig. 2 shows an overview of the AI modules within the fever screening system. We propose a novel cross-spectral generative adversarial network, called CS-GAN, which is a strategically modified version of CycleGAN [2]. Here, the input visual stream is our target domain, and we use known object detectors available for this domain to detect objects like face or person. We use the bounding box information of the visual object to form several candidate bounding box proposals in the thermal domain by using *adaptive spatial search*, which is discussed in Section II-E. This obviates the need for good object detectors in the thermal domain, where accurate object detection is not possible due to texture-less data. Since we only have good feature extractors for the target domain (visual) at our disposal, we transform images from the source domain (thermal) to the target domain (visual) by using CS-GAN.

A. Cross-Spectral GAN (CS-GAN)

CS-GAN has two networks. Fig. 3 shows the first network, which synthesizes visual images from thermal data. Second network transforms visual images into the thermal domain. Our experimental results (reported later) show CS-GAN can achieve state-of-the-art generation quality, with lower Fréchet Inception Distance.

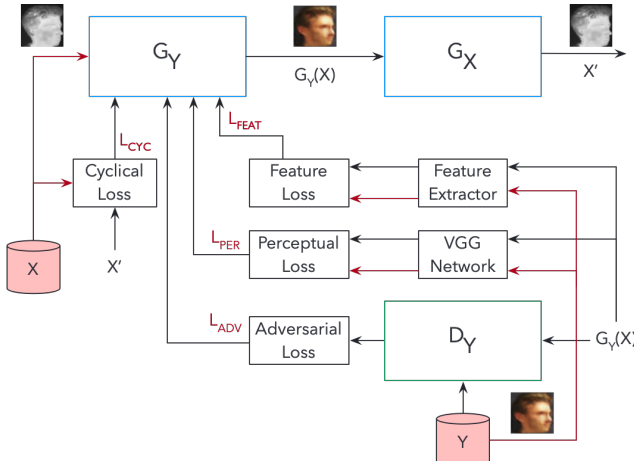


Figure 3: Thermal to visual synthesis

1) *Thermal to visual synthesis*: Fig. 3 shows our network to synthesize visual images from thermal data. Given a thermal patch (bounding-box), our generator synthesizes visual images that satisfy a key goal: synthesized images should conserve spatial information in the thermal patch, and retain key object features and landmarks. On the other hand, our discriminator learns to judge whether the synthesized visual images are visually homogeneous and have key object features.

Given a thermal image X , the generator G_Y synthesizes a synthetic visual image $G_Y(X)$. Synthetic visual images are

used for training the discriminator D_Y , which is able to distinguish between the original visual image Y and the synthesized visual image $G_Y(X)$. Discriminator network is able to predict whether the synthesized image is real or fake, and its output allows for computation of adversarial loss, which is required to train the discriminator and generator networks. Generator G_X is used to reconstruct the original thermal image from the synthesized visual image $G_Y(X)$. Reconstructed thermal image is $X' = G_X(G_Y(X))$. The difference between the original thermal image and the synthesized thermal image (i.e. between X, X') is used to compute the cyclical loss, which is necessary to train generator networks G_Y & G_X for cyclic consistency.

2) *Visual to thermal synthesis*: This process also uses a generator and a discriminator. Again, we use adversarial loss to train generator G_X and discriminator D_X . For cyclical loss, we calculate the $L1$ norm between the real Y and the reconstructed visual image $Y' = G_Y(G_X(Y))$. Perceptual loss is calculated from real and synthesized thermal images ($X, G_X(Y)$).

B. Loss functions

1) *Overall Objective Function*: The overall objective function L is a weighted sum of four loss functions.

$$\begin{aligned} \mathbb{L}(G_Y, G_X, D_Y, D_X) = & \mathbb{L}_{ADV}(G_Y, G_X, D_Y, D_X, X, Y) \\ & + \lambda_{cyc} \mathbb{L}_{CYC}(G_Y, G_X, X, Y) \\ & + \lambda_{per} \mathbb{L}_{PER}(G_Y, G_X, X, Y) \\ & + \lambda_{feat} \mathbb{L}_{FEAT}(G_Y, X, Y) \end{aligned} \quad (1)$$

where λ_{cyc} , λ_{per} and λ_{feat} are weights for cyclical, perceptual and feature preserving losses respectively.

Adversarial (L_{ADV}) and cyclical (L_{CYC}) loss functions are the same as the CycleGAN loss functions [2]. The perceptual (L_{PER}) is similar to [3]. Feature-preserving (L_{FEAT}) loss functions are new, and it is described here.

2) *Feature-preserving loss*: To ensure that synthesized images retain important features, we propose a new *feature-preserving loss* function, which helps retain the higher-level object features (like the facial landmarks, for example). This also makes CS-GAN to be feature-point-centric. This enables the generator to produce textured synthetic images, which makes it easy to detect various objects and associated landmarks with higher accuracy (Table I). Given a batch size m and k feature points, we define feature-preserving loss as follows:

$$\begin{aligned} FPL_i &= \sum_{j=1}^k \|f_p(y_{i,j}) - f_p(G_Y(x_{i,j}))\|_2 \\ \mathbb{L}_{FEAT}(G_Y, Y, X) &= \begin{cases} \frac{1}{m} \sum_{i=1}^m FPL_i & , \text{if } mRatio < t_{feat} \\ 0 & , \text{otherwise} \end{cases} \end{aligned} \quad (2)$$

Here, $f_p(G_Y(x))$ and $f_p(y)$ are feature points from synthesized and real images, respectively; $f_p \in \mathbb{R}^2$ are coordinates of

feature points in an image, t_{feat} is the threshold beyond which loss is added and $mRatio$ is $\frac{\# \text{ of images with no features}}{\text{batchsize}}$.

C. Dual bottleneck residual block

Vanishing gradients are a common problem in deeper networks. Gradients start getting smaller and smaller as they are back-propagated to earlier layers due to chain multiplication of partial derivatives.

We propose Dual Bottleneck Residual Block (Dual-BRB) (Fig. 4), which consists of 4 convolutional blocks as $G_{(1 \times 1)}$, $F_{(3 \times 3, 3 \times 3)}$ and $H_{(1 \times 1)}$. The function G squeezes number of channels reducing computation for function $F(\cdot)$. Then function $H(\cdot)$ expands channels similar to input channels. All blocks have full pre-activation. We have two skip connections in Dual-BRB. Inner skip connection is an identity mapping for function $F(\cdot)$, while outer skip connection provides identity mapping for complete block.

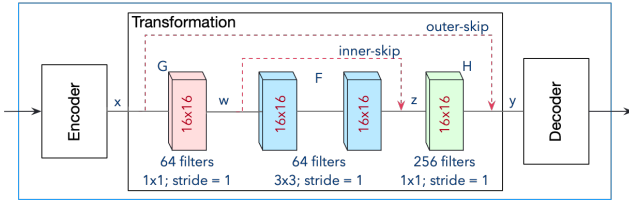


Figure 4: Dual Bottleneck Residual Block

$$w = G(x), \quad z = F(w) + w$$

$$y = H(z) + x = H(F(G(x)) + G(x)) + x$$

where y is output from Dual-BRB. Inner skip connection across $F(\cdot)$ helps in learning residual across it, while helping in model robustness and convergence.

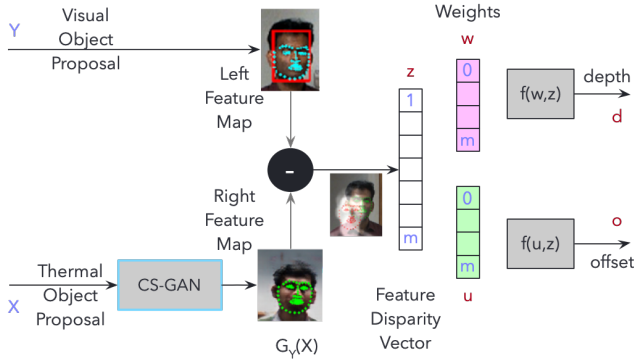


Figure 5: Depth and Offset Estimator

D. Inferencing

During inferencing, CS-GAN accepts thermal object image tiles, which are obtained from adaptive spatial search and fed to generator G_Y , which in turn transforms them into synthesized, visual spectrum images that retain structural information.

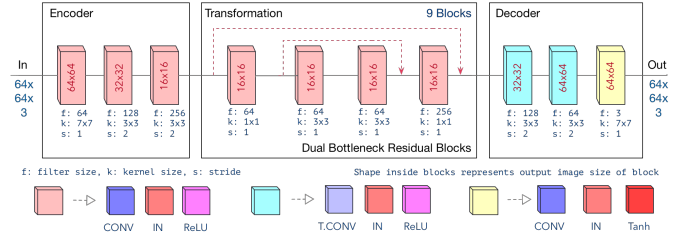


Figure 6: Network architecture of Generator

E. Depth & Offset Estimator

Fig. 5 shows the procedure followed to estimate depth and offset of an individual relative to the sensor, which is required to compensate for temperature variation based on the distance. After bounding boxes of objects are identified in the visual domain, an adaptive spatial search method determines candidate object proposals in the thermal domain. This process depends on sensor displacement, sensor fields of view, zoom levels, resolutions and relative orientation. Consider an image Y with k objects, $\{y_i\}_{i=1}^k$. Let the thermal image be X , and the thermal bounding box proposals be $B_{x_i} = \Phi(B_{y_i})$ where Φ maps a bounding box in visual domain to an estimated bounding box in thermal image.

Adaptive search also depends on baseline (distance separating the cameras) b , which determines offset, angle of view and image resolution. We compute the function Φ by using the ratio of focal lengths of cameras and offset. Let pairs (R_Y, R_X) and (f_Y, f_X) represent resolution and focal length of visual and thermal imaging sensor. Given $\Phi \propto (f, R)$, a heuristic bounding box is estimated as $B_x = f_x B_y / f_y \pm \hat{b}$, where \hat{b} is horizontal offset. Using thermal object proposals B_x , visual object proposals B_y are expanded, so that each visual (y_i) and corresponding thermal (x_i) cropped proposals have same size. As the next step, landmark detection is performed on y_i and feature vector y_i is extracted. Since landmark detection cannot be performed directly on x , it is converted to $G_Y(x_i)$ using CS-GAN. Landmark detection is performed on $G_Y(x_i)$ and a feature vector \hat{y}_i is extracted.

Let z be object feature disparity vector. z consists of euclidean distances between n -feature points and angle between n -feature points, i.e., $z = (\|y - \hat{y}\|_2, \text{atan}(y, \hat{y}))$ where $z \in \mathbb{R}^m$ and $m = 2n$. We regress distance (d) from sensors and offset (o) and train a multivariable linear regressor by using $2n$ explanatory variables. The regressor minimizes residual sum of squares. If the coefficients of distance-estimator model are $w \in \mathbb{R}^{m+1}$, and offset-estimator coefficients are $u \in \mathbb{R}^{m+1}$, then the object distance and offset are estimated as follows:

$$d = w_0 + \sum_{j=1}^m w_j z_j + \hat{\epsilon}_d = w^T z + \hat{\epsilon}_d \quad (3)$$

$$o = u^T z + \hat{\epsilon}_o \quad (4)$$

where $\hat{\epsilon}_d$ and $\hat{\epsilon}_o$ are distance and offset residuals.

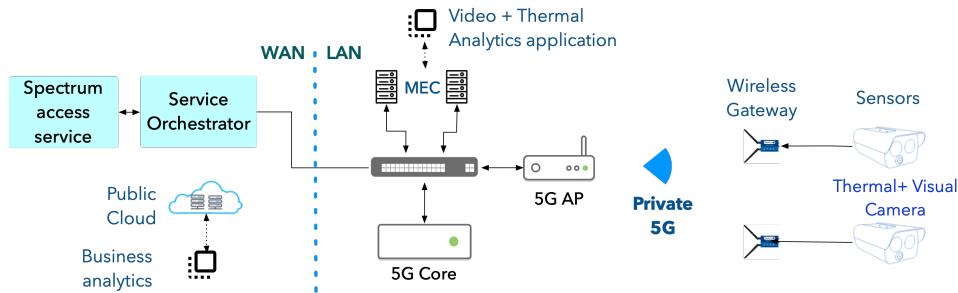


Figure 7: Deployment architecture

III. EXPERIMENTAL SETUP

A. Compute and Communication Network setup

Private 5G which is also known as a local or non-public 5G network, is LAN which uses 5G technologies to create a dedicated network with unified connectivity, optimized services and a secure means of communication within a specific physical area. It delivers the speed, latency and other benefits promised by 5G to applications. Our system utilizes Band 48 (CBRS) in 3.5 GHz spectrum. It spans between 3550 MHz to 3700 MHz range, under Tier 3 Priority Access License (PAL).

CBRS (Citizens Broadband Radio Service) allows economic way for businesses to deploy private LTE and 5G network in their premises. It provides better indoor and outdoor cellular signal with enhanced security. We have used both indoor and outdoor Access Points to form local cellular network. Thermal and RGB cameras are connected to cellular network using ethernet-to-cellular bridge devices. Overview of our deployment is shown in Fig. 7.

We have used combination of Multitech [4] and Cradlepoint [5] wireless gateways to connect Customer Premise Equipment (CPE) devices over private 5G to Access Points from Celona [6]. These access points provide coverage for upto 25K SQFT indoor area and 1M SQFT outdoor area. Spectrum Access System (SAS) is provided by Federated Wireless [7]. Deployment of devices at the edge is managed through Celona’s Service Orchestrator, which resides in the cloud. Along with initial deployment, Service Orchestrator also provides functions for routine maintenance and any policy related automation. Our Multi-access Edge Computing (MEC) [8] server setup consists of one master node server with 10-core Intel core i9 CPU and five worker node servers equipped with 24-core Intel CPUs.

B. Generator Network architecture

Fig. 6 shows architecture of our generator network, which consists of an encoder, a transformer and a decoder block. Encoder network consists of a 7×7 convolution layer, followed by down-sampling layers using two 3×3 convolution (stride-2). Dual-BRBs reduce inference time by a factor of 2 when compared with basic residual block implementation in [9], and inference speed is achieved without degrading image quality (Fig. 8a). The final decoder network consists of two up-sampling layers of 3×3 transpose convolution (T.CONV) and a

final 7×7 convolution layer with \tanh activation. Discriminator networks D_Y and D_X are similar to [10].

C. Training

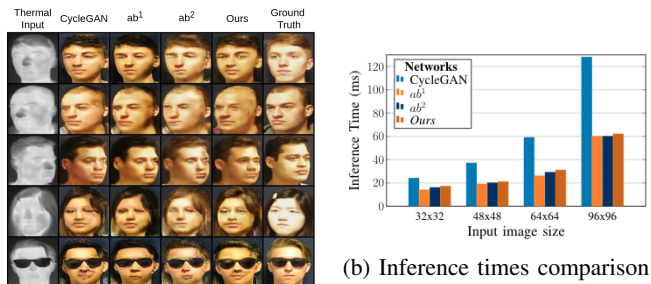
Training was done on an Intel Core i9-9900K CPU @ 3.6 GHz, which has an Nvidia GeForce RTX 2070 GPU with 8GB Memory. Image pre-processing like cropping and resizing of images was followed by normalization. An image size of 64×64 was used across all experiments. Thermal data was converted from 1 channel to 3 channels to keep it consistent with 3 channels in visual image. We used $\lambda_{cyc} = 10$, $\lambda_{per} = 4.0$ and $\lambda_{feat} = 7.0$ in the overall objective function (1). Adam Optimizer was used with parameters as $\alpha = 0.0002$, $\beta_1 = 0.5$ and $\beta_2 = 0.999$. We start decaying learning rate based on feature preserving loss.

D. Datasets

We used proprietary data for training, and public data for validation and testing.

Proprietary data: We collected extensive facial images from Intel Real-sense and Mobotix M16-TR thermal camera during our field trials. Person and face image pairs are labeled with distance and offset measurements using Intel RealSense.

Public data - IRIS [11]: It has paired thermal images and visible images for faces with various poses, expressions and illuminations.



(a) Image quality comparison

(b) Inference times comparison

Figure 8: Analysis of Dual Bottleneck Residual Blocks

IV. RESULTS

A. Dual Bottleneck Residual Blocks

Qualitative analysis: In Fig. 8a, we compare image quality across different networks. The first network is CycleGAN

with *Basic Residual Block*. The second network ab^1 is an ablation of proposed network, where we use *Basic Bottleneck Residual Block* instead of Basic Residual block. This usage is similar to [9]. The third network ab^2 is another ablation of proposed network, but with *Single Skip Bottleneck Residual Block*. The fourth network is the proposed Dual-BRBs. We could not reliably detect landmark features from all images synthesized by CycleGAN, ab^1 or ab^2 networks. However, our landmark detector was able to detect landmarks across all images synthesized by CS-GAN.

Quantitative analysis: We measured transformation times [Intel Core i7-8650U CPU @ 1.9 GHz] for various input image sizes. As shown in Fig. 8b, inference time is about 31 ms to transform 64x64 thermal image into synthetic visual image. This performance is good enough for real-time applications.

B. Loss functions

Qualitative analysis: We evaluated following combinations of loss functions: (a) No Perception loss (P) + No Landmark Loss (LM) + No Object detector (OD) loss, (b) With P + No LM + No OD, (c) With P + No LM + With OD, (d) With P + With 5-LM + With OD, and (ours) (proposed overall loss function) With P + With 68-LM + With OD.

Quantitative analysis:

Table I: Impact of ablated loss functions on synthesized images

Evaluation Metrics	(a)	(b)	(c)	(d)	(e)
Face Detector Accuracy	0.94	0.96	0.96	0.97	0.97
Feature Detector Error	28.8	19.7	19.1	16.7	16.3
FID Score	85	55	53	39	37

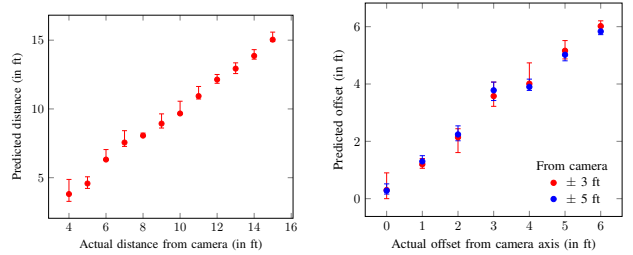
Our results shown in Table I confirm our method is able to synthesize visual images that yield higher object detector accuracy, lower error, and lower FID score by using proposed overall loss function, when compared with other ablated versions.

C. Comparison with other methods

We compare our framework with three baselines: CycleGAN [2], TV-GAN [12], TR-GAN [13]. Our framework is able to generate visual object counterparts, with better object detection accuracy (0.98), with lower errors. The proposed network CS-GAN produces realistic visual images under diverse conditions in realtime, at 30ms for 64x64 image. We also compared our method of object position estimation with pixel-wise stereo disparity method using KITTI dataset, wherein total processing time is around 18.1 seconds. Using our method, it takes only 73 milliseconds per frame (using similar hardware as pixel-wise method described above), achieving real-time processing.

D. Evaluation of depth & offset estimation

We analyzed our system with people standing at different distances and offsets from sensors and compared against ground truth. There is negative correlation between distance



(a) Actual vs predicted distance (b) Actual vs predicted offset

Figure 9: Depth and Offset Evaluation

Table II: Accuracy (Edge vs Cloud)

Deployment	TP	FP	TN	FN	Accuracy
Cloud (AWS)	6	2	110	24	81.6%
Edge (MEC + private 5G)	7	1	133	1	98.5%

from sensors and difference in pixels between two cross-spectral images. As shown in Fig. 9a and 9b, observed and model’s predicted distance and offset are strongly correlated.

E. Accuracy - Edge vs Cloud

Ability to process all the faces in the sensor’s field of view reliably, depends on available bandwidth and latency between the sensor and backend system. Table II shows accuracy [14] of fever screening system, when the modules are deployed on a centralized cloud vs when they are deployed at the edge. Note that we measured the accuracy under same lighting and environmental conditions, with people of different age, gender, race, skin color, etc. moving either alone or together in a group. Our focus here is compare accuracy of fever screening system under same conditions, when the modules are deployed at the edge or on the cloud. We can see that the accuracy is higher at the edge compared to the cloud, because there is less network delay, which results in more frames being processed, thereby increasing the accuracy.

F. Throughput - Edge vs Cloud

Higher the throughput i.e. number of people that are screened per minute, the better it is, since it avoids crowding, which can lead to spread of the virus. Table III shows the throughput when fever screening modules are deployed on a centralized cloud vs when they are deployed at the edge, as people walk through at a normal pace of about 1 meters/s. We can see that the throughput is higher ($\sim 5X$) when modules are deployed at the edge, since the processing for each person is much quicker due to proximity of edge resources.

V. RELATED WORK

Methods like modified SIFT (gradient invariant SIFT- GD SIFT) [15], multi-oriented Log-Gabor filters (Log-Gabor histogram descriptor - LGHD) [16] and dense adaptive self-correlation (DASC) [17] have been proposed for cross-spectral correspondence, but these methods are not robust or accurate. Conversion of thermal frame into visible spectrum has

Table III: Throughput (Edge vs Cloud)

Deployment	Throughput
Cloud (AWS)	14 persons/min
Edge (MEC + private 5G)	66 persons/min

been explored in ThermalGAN [18], TV-GAN [12] and TR-GAN [13] for cross-modal face recognition. However, these networks do not meet real-time constraints.

Many stereo object localization algorithms [19] compute pixel-wise disparity between stereo images and they generate point clouds. Creating cross spectral object detection models for point clouds needs lot of labelled data, which is challenging. In contrast, the proposed cross-spectral object depth and offset estimator generates object-level disparity maps in real-time (Section II-E).

Mobile edge computing (MEC) enables a range of applications [20] e.g. driver-less vehicles, VR/AR, robotics and immersive media. Various private 5G enabled IoT edge applications in domain of industrial automation and healthcare are discussed in [21]. Similar to these, we leverage MEC and 5G for an application in healthcare domain i.e. fever screening system, to identify and isolate individuals with fever.

VI. CONCLUSION

We propose an edge-based fever screening system, which leverages edge computing and 5G, and uses our novel cross-spectral generative adversarial network (CS-GAN) to achieve real-time fever screening of individuals. Our system is able to achieve 98.5% accuracy and is able to process $\sim 5X$ more persons per minute compared to a centralized cloud deployment.

REFERENCES

- [1] Y. Cui, R. Chen, W. Chu, L. Chen, Y. Li, and D. Cao, "Deep learning for image and point cloud fusion in autonomous driving: a review," 2020. [Online]. Available: <http://arxiv.org/pdf/2004.05224.pdf>
- [2] J. Zhu, T. Park, P. Isola, and A. A. Efros, "Unpaired image-to-image translation using cycle-consistent adversarial networks," *CoRR*, vol. abs/1703.10593, 2017. [Online]. Available: <http://arxiv.org/abs/1703.10593>
- [3] J. Johnson, A. Alahi, and F. Li, "Perceptual losses for real-time style transfer and super-resolution," *CoRR*, vol. abs/1603.08155, 2016. [Online]. Available: <http://arxiv.org/abs/1603.08155>
- [4] "Multitech." [Online]. Available: <https://www.multitech.com/brands/multiconnect-ecell>
- [5] "Cradlepoint." [Online]. Available: <https://cradlepoint.com/technology/private-lte/>
- [6] "Celona." [Online]. Available: <https://celona.io/>
- [7] "Federated wireless SAS." [Online]. Available: <https://www.federatedwireless.com/tag/spectrum-access-system/>
- [8] T. X. Tran, A. Hajisami, P. Pandey, and D. Pompili, "Collaborative mobile edge computing in 5G networks: New paradigms, scenarios, and challenges," *IEEE Communications Magazine*, vol. 55, no. 4, pp. 54–61, 2017.
- [9] K. He, X. Zhang, S. Ren, and J. Sun, "Deep residual learning for image recognition," *CoRR*, vol. abs/1512.03385, 2015. [Online]. Available: <http://arxiv.org/abs/1512.03385>
- [10] P. Isola, J. Zhu, T. Zhou, and A. A. Efros, "Image-to-image translation with conditional adversarial networks," *CoRR*, vol. abs/1611.07004, 2016. [Online]. Available: <http://arxiv.org/abs/1611.07004>
- [11] B. Abidi, "Iris thermal/visible face database," 2012, university of Tennessee. [Online]. Available: <http://vcipl-okstate.org/pbvs/bench/Data/02/download.html>
- [12] T. Zhang, A. Wiliem, S. Yang, and B. C. Lovell, "TV-GAN: generative adversarial network based thermal to visible face recognition," *CoRR*, vol. abs/1712.02514, 2017. [Online]. Available: <http://arxiv.org/abs/1712.02514>
- [13] L. Kezebou, V. Oludare, K. Panetta, and S. Agaian, "TR-GAN: thermal to RGB face synthesis with generative adversarial network for cross-modal face recognition," in *Mobile Multimedia/Image Processing, Security, and Applications 2020*, S. S. Agaian, V. K. Asari, S. P. DelMarco, and S. A. Jassim, Eds., vol. 11399, International Society for Optics and Photonics. SPIE, 2020, pp. 158 – 168. [Online]. Available: <https://doi.org/10.1117/12.2558166>
- [14] J. Davis and M. Goadrich, "The relationship between precision-recall and roc curves," in *Proceedings of the 23rd International Conference on Machine Learning*, ser. ICML '06. New York, NY, USA: Association for Computing Machinery, 2006, p. 233–240. [Online]. Available: <https://doi.org/10.1145/1143844.1143874>
- [15] D. Firmenichy, M. Brown, and S. Süssstrunk, "Multispectral interest points for rgb-nir image registration," in *2011 18th IEEE International Conference on Image Processing*, 2011, pp. 181–184.
- [16] C. A. Aguilera, A. D. Sappa, and R. Toledo, "Lghd: A feature descriptor for matching across non-linear intensity variations," in *2015 IEEE International Conference on Image Processing (ICIP)*, 2015, pp. 178–181.
- [17] S. Kim, D. Min, B. Ham, M. N. Do, and K. Sohn, "Dasc: Robust dense descriptor for multi-modal and multi-spectral correspondence estimation," *IEEE Transactions on Pattern Analysis and Machine Intelligence*, vol. 39, no. 9, pp. 1712–1729, 2017.
- [18] V. V. Kniaz, V. Knyaz, J. Hladůvka, W. Kropatsch, and V. Mizginov, "Thermalgan: Multimodal color-to-thermal image translation for person re-identification in multispectral dataset," in *ECCV Workshops*, 2018.
- [19] J. Chang and Y. Chen, "Pyramid stereo matching network," *CoRR*, vol. abs/1803.08669, 2018. [Online]. Available: <http://arxiv.org/abs/1803.08669>
- [20] Q.-V. Pham, F. Fang, V. N. Ha, M. J. Piran, M. Le, L. B. Le, W.-J. Hwang, and Z. Ding, "A survey of multi-access edge computing in 5G and beyond: Fundamentals, technology integration, and state-of-the-art," *IEEE Access*, vol. 8, pp. 116974–117017, 2020.
- [21] A. Narayanan, A. S. D. Sena, D. Gutierrez-Rojas, D. C. Melgarejo, H. M. Hussain, M. Ullah, S. Bayhan, and P. H. J. Nardelli, "Key advances in pervasive edge computing for industrial internet of Things in 5G and Beyond," *IEEE Access*, vol. 8, pp. 206734–206754, 2020.